

Nature of charge density waves and superconductivity in

$1T\text{-TaSe}_{2-x}\text{Te}_x$

Y. Liu,^{1,*} D. F. Shao,^{1,*} L. J. Li,¹ W. J. Lu,^{1,†} X. D. Zhu,² P. Tong,¹ R. C. Xiao,¹ L. S. Ling,² C. Y. Xi,² L. Pi,² H. F. Tian,³ H. X. Yang,^{3,‡} J. Q. Li,^{3,4} W. H. Song,¹ X. B. Zhu,¹ and Y. P. Sun^{2,1,5,§}

¹*Key Laboratory of Materials Physics,
Institute of Solid State Physics, Chinese Academy of Sciences,
Hefei 230031, People's Republic of China*

²*High Magnetic Field Laboratory, Chinese Academy of Sciences,
Hefei 230031, People's Republic of China*

³*Beijing National Laboratory for Condensed Matter Physics,
Institute of Physics, Chinese Academy of Sciences,
Beijing 100190, People's Republic of China*

⁴*Collaborative Innovation Center of Quantum Matter,
Beijing, 100190, People's Republic of China*

⁵*Collaborative Innovation Centre of Advanced Microstructures,
Nanjing University, Nanjing 210093, People's Republic of China*

Abstract

Transition-metal dichalcogenides (TMDs) MX_2 ($M = \text{Ti, Nb, Ta}$; $X = \text{S, Se, Te}$) exhibit a rich set of charge density wave (CDW) orders, which usually coexist and/or compete with superconductivity. The mechanisms of CDWs and superconductivity in TMDs are still under debate. Here we perform an investigation on a typical TMD system, $1T\text{-TaSe}_{2-x}\text{Te}_x$ ($0 \leq x \leq 2$). Doping-induced disordered distribution of Se/Te suppresses CDWs in $1T\text{-TaSe}_2$. A domelike superconducting phase with the maximum T_c^{onset} of 2.5 K was observed near CDWs. The superconducting volume is very small inside the CDW phase and becomes very large instantly when the CDW phase is fully suppressed. The observations can be understood based on the strong q -dependent electron-phonon coupling-induced periodic-lattice-distortion (PLD) mechanism of CDWs. The volume variation of superconductivity implies the emergence of domain walls in the suppressing process of CDWs. Our concluded scenario makes a fundamental understanding about CDWs and related superconductivity in TMDs.

“Unconventional superconductivity” refers superconductivity cannot be explained by the conventional electron-phonon coupling mechanism. Usually, unconventional superconductivity appears near the boundary of an ordered phase with broken translational or spin rotation symmetry¹⁻³, so that it is thought to be tightly related to a (purely electronic) quantum critical point (QCP)^{4,5}. Transition metal dichalcogenides (TMDs) MX_2 , where $\text{M} = \text{Ti, Nb, Ta, etc.}$, and $\text{X} = \text{S, Se, Te}$, exhibit a rich set of Peierls-like charge density wave (CDW) orders⁶. Many typical TMDs show the coexistence and/or competition between conventional superconductivity and CDW⁷⁻¹⁶. The resulted phase diagrams are very similar to those of unconventional superconductors, indicating that such superconductivity might be potentially due to a new kind of QCP unrelated to magnetic degrees of freedom¹⁷⁻¹⁹. However, QCP is found to be far away from superconductivity recently in $1T\text{-TiSe}_2$ under pressure²⁰.

A better understanding of the relation needs to figure out the origin of CDW, which is a rather old but still long-standing issue in condensed matter physics²¹⁻²³. The CDW and accompanied period-lattice-distortion (PLD) are usually explained by Peierls picture²¹⁻²⁴: Fermi surface nesting, a pure electronic effect, drives the charge redistribution regardless of whether or not PLD subsequently happens. There is an opposite mechanism that the charge redistribution is driven by strong \mathbf{q} -dependent electron-phonon coupling induced PLD, while Fermi surface nesting only plays a minor role^{24,25}.

The typical system $1T\text{-TaX}_2$ ($\text{X} = \text{S, Se, Te}$) (Figs. 1 (a)-(c)) is a good platform to investigate CDW and superconductivity. Some reports suggested Fermi surface nesting leads to CDW in the system^{6,26-30}, while some other investigations supported PLD mechanism^{31,32}. Making solid solution of different parent materials of the system and observing the variation of CDW vector might help to figure out the universal CDW mechanism. Moreover, the correlation effect opens Mott gap of $5d$ -band of Ta in commensurate (C) CDW in $1T\text{-TaX}_2$ ($\text{X} = \text{S, Se}$)¹⁵. Suppression of CCDW in $1T\text{-TaS}_2$ leads to a unique nearly commensurate (NC) CDW ground state, which is composed of metallic incommensurate (IC) network and Mott insulating CCDW domains⁶. Superconductivity emerges only in the percolated metallic interdomain area^{8,12-14}, which is clearly not related to the QCP. On the other hand, at low temperatures $1T\text{-TaSe}_2$ exhibits CCDW the same as $1T\text{-TaS}_2$ does⁶. However, no NCCDW phase has been found in $1T\text{-TaSe}_2$. Introducing superconductivity into $1T\text{-TaSe}_2$ and comparing it with the superconductivity in $1T\text{-TaS}_2$ might lead to a better

understanding of the universal relation of CDW and superconductivity in TMDs.

Previously, we found that the isovalent substitution in $1T$ -TaS_{2-x}Se_x ($0 \leq x \leq 2$) system suppresses CCDW and NCCDW accompanied with superconductivity emergence in the middle doping area^{14,15,33}. An ordered stacking of S/Ta/Se sandwiches is observed in $1T$ -TaSSe³³. In the present work, we prepared a series of $1T$ -TaSe_{2-x}Te_x ($0 \leq x \leq 2$) single crystals and obtained a phase diagram through the transport measurements. Different from the case in $1T$ -TaS_{2-x}Se_x, we found that the doping induces Se/Te disorder in the system and suppresses CDW when $0.5 < x < 1.5$. A dome-like superconductivity with maximum T_c^{onset} of 2.5 K was observed near CDW. The superconducting volume is very small inside the CDW phase and becomes very large instantly when CDW is fully suppressed. Our observations can be clearly understood based on PLD mechanism. The volume variation of superconductivity implies the emergence of domain walls when CDW is suppressed.

SUPERCONDUCTING DOME NEAR CDW

The X-ray diffraction (XRD) patterns of $1T$ -TaSe_{2-x}Te_x ($x = 0, 1$, and 2) single crystals are shown in Fig. 1 (d), in which only (00l) reflections were observed, suggesting the c -axis is perpendicular to the surface of single crystal. With increasing x , the diffraction peaks distinctly shift to lower angles, reflecting the crystal expansion induced by Te doping. Figure 1 (e) shows the powder XRD patterns and the structural refinement results of Rietveld analysis for the selected samples with $x = 0, 1$, and 2 . Figure 1 (f) shows the enlargement of the (011) peak for $x = 1, 1.5$, and 2 . The undistorted CdI₂-type $1T$ structure for $x = 1$ leads to a single (011) peak, while there are double peaks resulting from the monoclinic distorted- $1T$ structure for $x = 2$. The (011) peak starts to split when $x = 1.5$, indicating the emergence of distorted- $1T$ structure, as shown in Fig. 1 (c). The evolution of lattice parameters ($a/b, c$) and unit cell volume (V) of $1T$ -TaSe_{2-x}Te_x are depicted in Fig. 1 (g). Indeed, the values of a, c , and V monotonously increase with x , in accordance with the larger ion radius of Te than that of Se.

Figures 1 (h) and (i) demonstrate two typical diffraction patterns taken along the [001] zone-axis direction of $1T$ -TaSe₂ and $1T$ -TaSeTe, respectively. The superstructure reflections corresponding to the commensurate phase with $\mathbf{q}_{\text{CCDW}} = \frac{3}{13}\mathbf{a}^* + \frac{1}{13}\mathbf{b}^*$ can be clearly observed in Fig. 1 (h), which is evidently different from the diffuse superlattice spots with

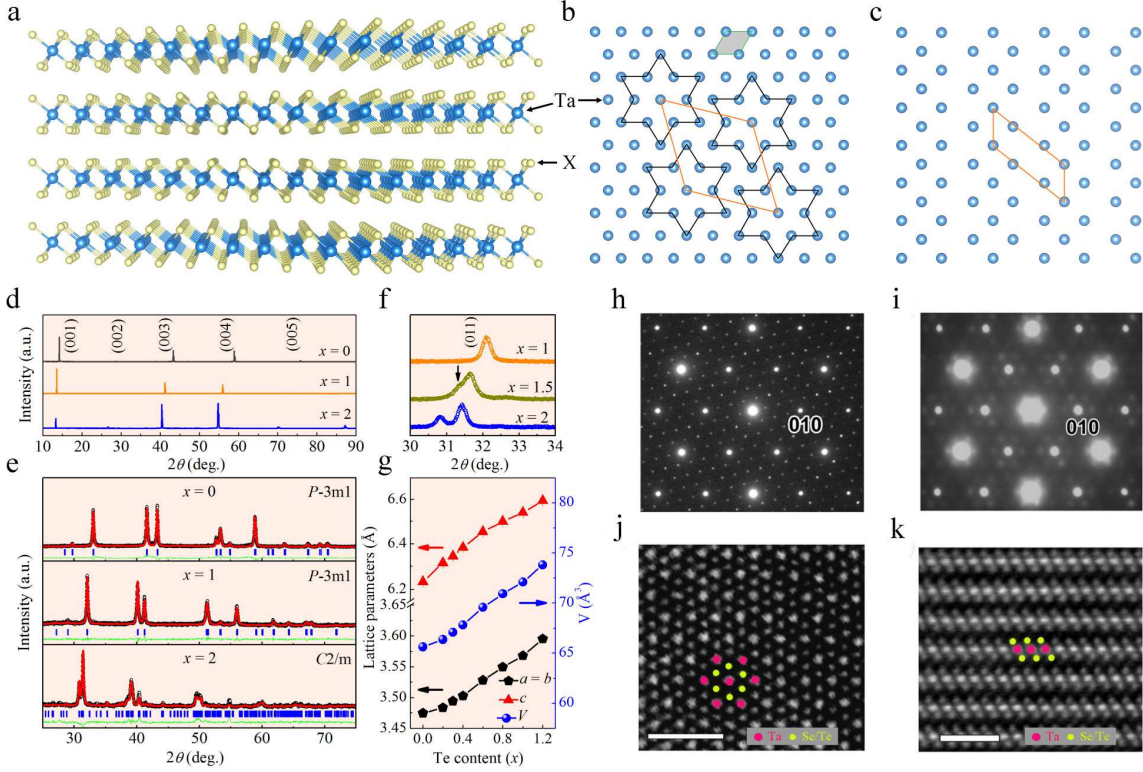


FIG. 1. **Structural information of $1T\text{-TaSe}_{2-x}\text{Te}_x$.** (a) Crystal structure of ideal $1T\text{-TaX}_2$ ($X = \text{S, Se, Te}$). (b) Top view of Ta plane in $1T\text{-TaX}_2$ ($X = \text{S, Se}$). At low temperatures, Ta atoms displace to make “David star” clusters, leading to 13.9° rotated $\sqrt{13} \times \sqrt{13}$ CCDW with $\mathbf{q}_{\text{CCDW}} = \frac{3}{13}\mathbf{a}^* + \frac{1}{13}\mathbf{b}^*$. (c) Top view of Ta plane in TaTe_2 . The monoclinic distorted- $1T$ structure of TaTe_2 can be seen as a 3×1 single- \mathbf{q} CDW-type distorted structure of hypothetical $1T\text{-TaTe}_2$ ^{6,29,30}. (d) Single-crystal XRD patterns of $1T\text{-TaSe}_{2-x}\text{Te}_x$ for $x = 0, 1$, and 2 , respectively. (e) Powder XRD patterns with Rietveld refinements of $1T\text{-TaSe}_{2-x}\text{Te}_x$ for $x = 0, 1$, and 2 , respectively. (f) The enlargement of the (011) peaks of the powder XRD patterns of $1T\text{-TaSe}_{2-x}\text{Te}_x$ for $x = 1, 1.5$, and 2 . (g) Evolution of lattice parameters (a, c) and cell volume (V) of $1T\text{-TaSe}_{2-x}\text{Te}_x$. Electron diffraction patterns of (h) $1T\text{-TaSe}_2$, and (i) $1T\text{-TaSeTe}$, taken along the [001] zone axis direction. HAADF STEM images of $1T\text{-TaSeTe}$ viewed from (j) [001] and (k) [100] zone axis direction. Scale bar, 1 nm.

incommensurated in-plane \mathbf{q} vector in $1T\text{-TaSeTe}$ (Fig. 1 (i)). Similar result was previously reported by Luo *et al.*³⁴ and a possible chemical origin, short-range Se/Te ordering was proposed. However, the detailed analysis based on the high-angle annular dark-field

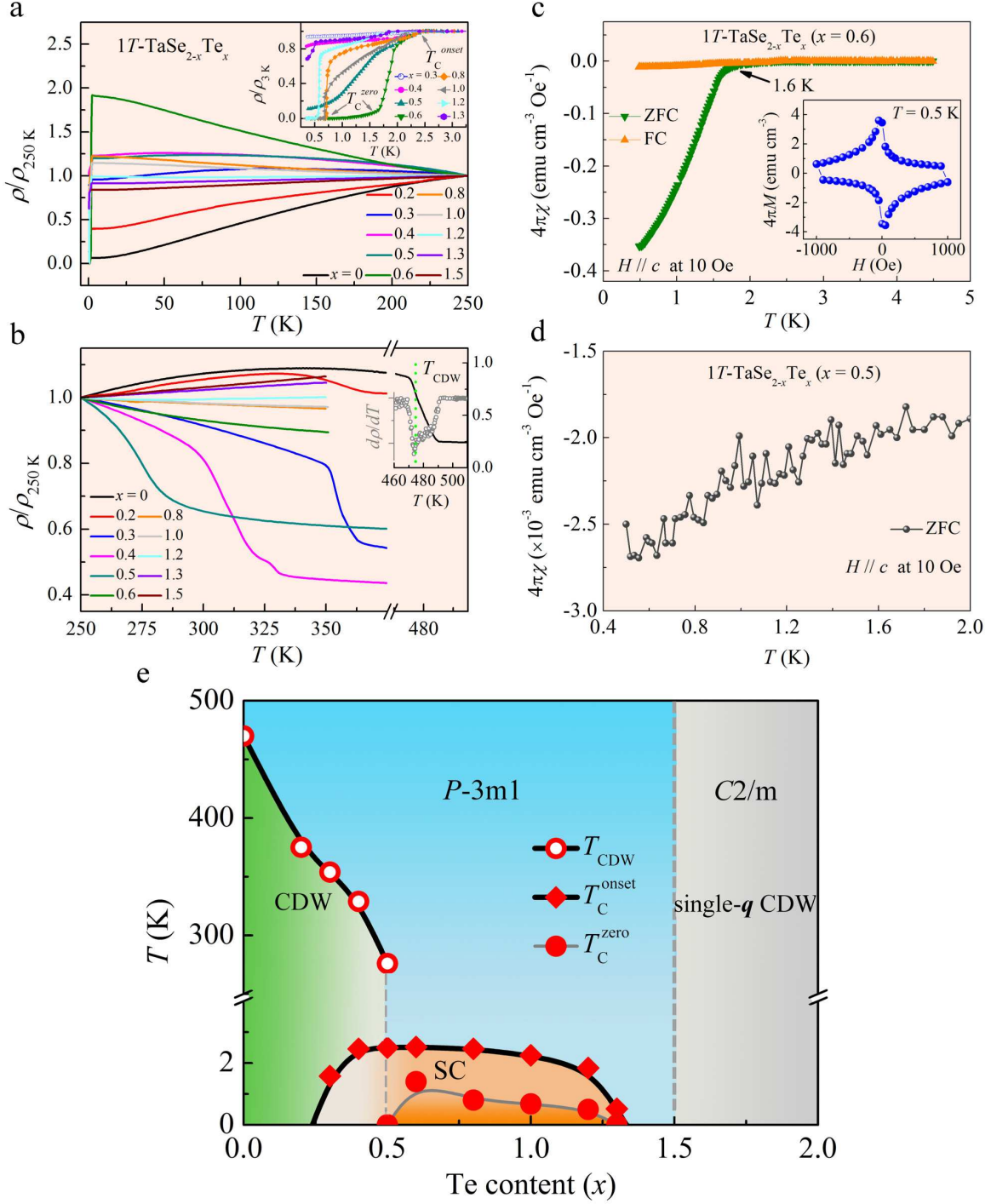


FIG. 2. **The phase diagram of $1T\text{-TaSe}_{2-x}\text{Te}_x$.** Temperature dependence of in-plane resistivity ratio ($\rho/\rho_{250\text{K}}$) of $1T\text{-TaSe}_{2-x}\text{Te}_x$ below $T = 250$ K (a) and above $T = 250$ K (b). Insets: the enlargement of superconducting transitions at low temperatures and the CCDW transition of $1T\text{-TaSe}_2$ at high temperatures. Temperature dependence of magnetic susceptibility ($4\pi\chi$) for $x = 0.6$ (c) and $x = 0.5$ (d). Inset: the magnetization hysteresis loop obtained at $T = 0.5$ K with magnetic field H paralleling c -axis. (e) Electronic phase diagram of $1T\text{-TaSe}_{2-x}\text{Te}_x$ as a function of temperature and Te content.

(HAADF) scanning transmission electron microscopy (STEM) images seen from both [001] (Fig. 1 (j)) and [100] (Fig. 1 (k)) zone axis directions suggest the disordered Se/Te distribution in the $1T$ -TaSeTe, which is significantly different from the ordered S/Se distribution in $1T$ -TaSSe³³.

Figures 2 (a) and (b) show the temperature dependence of in-plane resistivity ratio ($\rho/\rho_{250\text{K}}$) of $1T$ -TaSe_{2-x}Te_x single crystals. The Te doping largely decreases the residual resistivity ratio (RRR = $\rho_{300\text{K}}/\rho_{3\text{K}}$). For $1T$ -TaSe₂, RRR = 17.4. For $1T$ -TaSeTe, RRR = 0.85, reflecting the substantial doping induced disorder, which is corresponding to our HAADF-STEM observation. The signature of superconductivity emerges as $x \geq 0.3$, and finally disappears for $x \geq 1.3$, while the zero resistances are observed when $0.5 < x < 1.3$ (Fig. 2 (a)). The maximum of superconducting onset temperature (T_c^{onset}) of 2.5 K and the maximum of zero resistance temperature (T_c^{zero}) of 1.6 K are found when CDW is completely suppressed ($x = 0.6$). Figures 2 (c) and (d) show the magnetic properties of $1T$ -TaSe_{1.4}Te_{0.6} (optimal sample) and $1T$ -TaSe_{1.5}Te_{0.5} at $H = 10$ Oe with the magnetic field paralleling to the c -axis, respectively. The results indicate very small superconducting volume in $1T$ -TaSe_{1.5}Te_{0.5} (in which CDW still exists) and large superconducting volume in $1T$ -TaSe_{1.4}Te_{0.6} (in which CDW is just completely suppressed). The inset of Fig. 2 (c) shows the magnetization hysteresis loop $M(H)$ obtained at $T = 0.5$ K, which shows that $1T$ -TaSe_{1.4}Te_{0.6} is a typical type-II superconductor.

Figure 2 (e) summarizes the overall phase diagram as a function of temperature and doping level in $1T$ -TaSe_{2-x}Te_x. The dome-like superconducting phase is near the CDW phase, which is similar to that in $1T$ -TaS_{2-x}Se_x¹⁴. In the phase diagram, the CDW is gradually suppressed by Te doping and disappears as $x > 0.5$, which is quite different from the situation in $1T$ -TaS_{2-x}Se_x¹⁴. With higher Te content $x > 1.5$, the crystal structure gradually distorts to a monoclinic one with the $C2/m$ space group, which could also be considered as a single- \mathbf{q} CDW-type distortion^{6,30}.

MECHANISMS OF CDW AND SUPERCONDUCTIVITY

To explain our observation in $1T$ -TaSe_{2-x}Te_x system, we performed the first principle calculations (Fig. 3). We firstly calculated the two end members of $1T$ -TaSe₂ and hypothetical $1T$ -TaTe₂, respectively. The fully optimized structural parameters, listed in Table I,

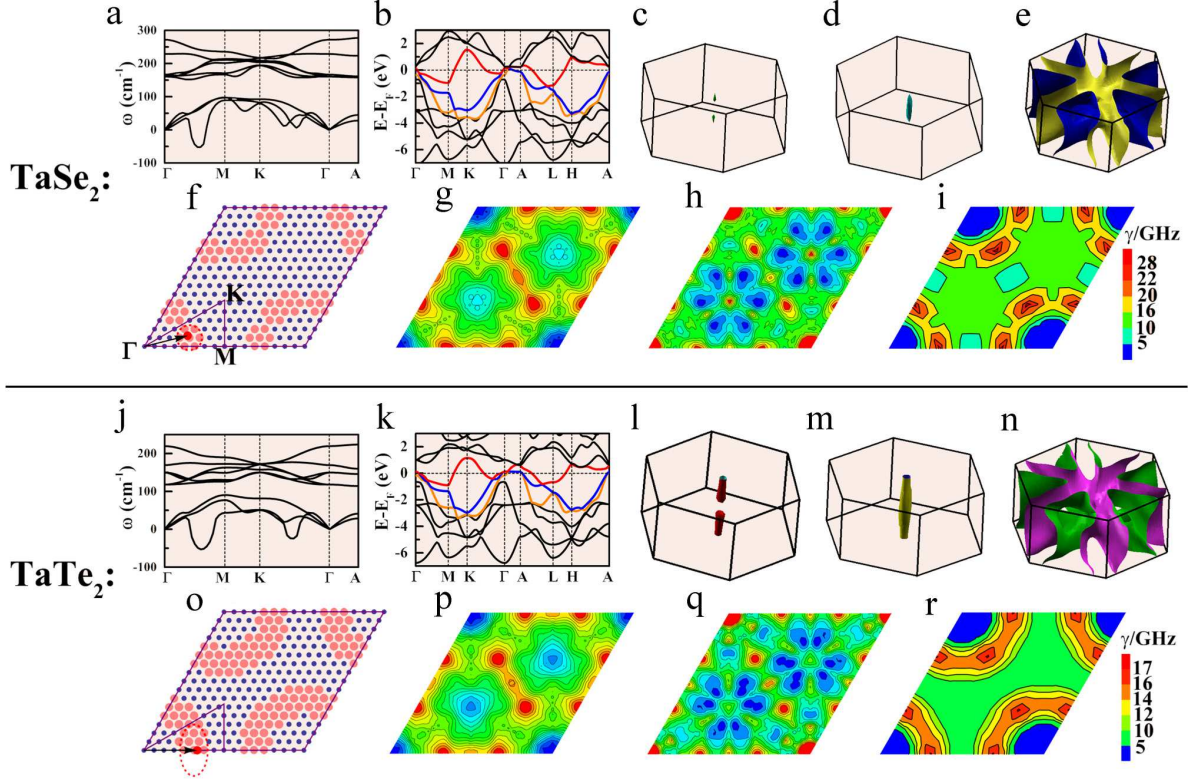


FIG. 3. **The first principles investigations on 1T-TaSe₂ and 1T-TaTe₂.** The top panel shows the phonon dispersions (a), band dispersions (b), Fermi surfaces (c)-(e), the distribution of instability in the $\mathbf{q}_z = 0$ plane (f), the cross section of real (g) and imaginary (h) parts of the generated electron susceptibility with $\mathbf{q}_z = 0$, and the contour map of the phonon linewidth γ of the lowest phonon modes in the $\mathbf{q}_z = 0$ of 1T-TaSe₂ (i). The bottom panel shows those of 1T-TaTe₂ ((j)-(r)). The bands crossing E_F are colored in (b) and (k). In (f) and (o), the pink solid circles denote the \mathbf{q} -points at which the frequency of the lowest mode is imaginary. The red solid circles and the black arrows in (f) and (o) denote the reported $\mathbf{q}_{\text{CCDW}} = \frac{3}{13}\mathbf{a}^* + \frac{1}{13}\mathbf{b}^*$ and $\mathbf{q} \approx \frac{1}{3}\mathbf{a}^*$ for 1T-TaSe₂ and 1T-TaTe₂, respectively. The high-symmetry K-points are shown in (f).

TABLE I. Structural parameters fully optimized by LDA for 1T-TaSe₂, 1T-TaSeTe(O), and 1T-TaTe₂.

	$a(\text{\AA})$	$c(\text{\AA})$	z_X
TaSe ₂	3.406	6.086	$z_{\text{Se}} = \pm 0.271$
TaTe ₂	3.622	6.572	$z_{\text{Te}} = \pm 0.274$
TaSeTe(O)	3.507	6.337	$z_{\text{Se}} = 0.249, z_{\text{Te}} = -0.296$

are close to those from the previous LDA calculation³². The underestimation of lattice parameters is expected for LDA³².

Previous researches showed the phonon calculation is an effective method to simulate the CDW instability^{29,31,32,35-37}. Figures 3 (a) and (j) show the phonon dispersions of 1*T*-TaSe₂ and 1*T*-TaTe₂. For 1*T*-TaSe₂, the calculation is in good agreement with the previous calculation by Ge *et al.*³². From Fig. 3 (f), one can notice that the calculated instability is just around the reported CCDW vector ($\mathbf{q}_{\text{CCDW}} = \frac{3}{13}\mathbf{a}^* + \frac{1}{13}\mathbf{b}^*$)²⁶. For 1*T*-TaTe₂, the area of instability is centered near $\mathbf{q}_{\text{CDW}} \approx \frac{1}{3}\mathbf{a}^*$ (Fig. 3 (o)), which is corresponding to the reported (3 × 1) single- \mathbf{q} CDW-type superlattice²⁹. The high coincidence of the calculated and experimentally reported instabilities strongly proves the reliability and accuracy of the phonon calculation. Moreover, different from 1*T*-TaSe₂, 1*T*-TaTe₂ shows a much larger area of instability, which expands to Γ K line (see Fig. 3 (j)). That might be the reason why 1*T*-TaSe₂ only shows the small atomic displacement in CDW phase, which can be suppressed at high temperatures, while the single- \mathbf{q} CDW-type distortion in TaTe₂ is very stable and the ideal-1*T* structure has never been observed.

Figures 3 (b) and (k) show the band structures and Fermi surfaces of 1*T*-TaSe₂ and 1*T*-TaTe₂, respectively. For 1*T*-TaSe₂, early calculations show there is only one band crossing Fermi energy (E_{F}), which does not cross E_{F} in the vicinity of Γ point^{27,38}. Moreover, there is a gap (about 0.1 ~ 0.2 eV) below the band crossing E_{F} ^{27,38}. However, the recent angle-resolved photoemission (ARPES) experiment clearly shows a hybridization of bands at Γ close to E_{F} , where small hole-type pockets are observed³⁹. Obviously, our LDA calculations accurately simulated the band structure of 1*T*-TaSe₂ (Fig. 3 (b)). Three bands cross E_{F} : The lower two bands (colored in blue and orange in Fig. 3 (b)) form small cylindrical hole-type pockets close to Γ (Figs. 3 (c) and (d)). The Fermi surface introduced from the higher band crossing E_{F} (colored in red in Fig. 3 (b)) is shown in Fig. 3 (e). 1*T*-TaTe₂, one can notice that the band structure and Fermi surfaces (Figs. 3 (k) - (n)) are highly similar to those of 1*T*-TaSe₂.

The Fermi surface nesting can be reflected in generated electron susceptibility²⁴. Figures 3 (g), (h), (p) and (q) show the cross section of the real part (χ') and imaginary part (χ'') of the electron susceptibility with $\mathbf{q}_{\text{z}} = 0$ for 1*T*-TaSe₂ and 1*T*-TaTe₂. We found that all the maxima of χ' and χ'' locate between Γ and M points. For 1*T*-TaSe₂, both the maxima of χ' and χ'' locate at $\mathbf{q} \approx \frac{1}{3}\mathbf{a}^*$. Earlier calculation by Myron *et al.*²⁸ shows a peak of χ' at

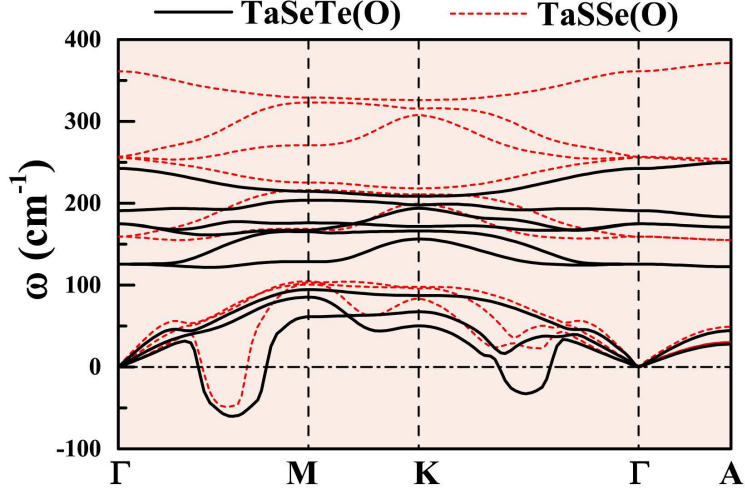


FIG. 4. Phonon dispersions of 1T-TaSeTe(O) and 1T-TaSSe(O).

$\mathbf{q} \approx 0.28\mathbf{a}^*$, while recent calculation by Yu *et al.*⁴⁰ reports a maximum of χ' at $\mathbf{q} \approx 0.295\mathbf{a}^*$. Clearly, the maxima of χ' and χ'' locate far away from $\mathbf{q}_{\text{CDW}} = \frac{3}{13}\mathbf{a}^* + \frac{1}{13}\mathbf{b}^*$. Therefore, Fermi surface nesting cannot account for the origin of CDW in 1T-TaSe₂.

We also calculated the electron-phonon coupling in the $\mathbf{q}_z = 0$ plane for 1T-TaSe₂ and 1T-TaTe₂. Figures 3 (i) and (r) show the calculated phonon linewidth γ of the lowest phonon modes in the $\mathbf{q}_z = 0$ plane. Although the calculation with $16 \times 16 \times 1$ \mathbf{q} -points is not enough to deduce the accurate vector with maximum γ , it can still qualitatively reflect the role of electron-phonon coupling. In the instability area, the γ of the lowest mode is hundreds times larger than those of higher modes, proving the connection between electron-phonon coupling and CDW. For 1T-TaSe₂, the biggest γ (~ 23.11 GHz) is found near the place where χ'' shows the maximum, which is understandable since Fermi surface nesting can enhance γ according to Eqs.(4) and (5) (Methods). The second largest γ (~ 22.18 GHz) is found in the place very near the reported $\mathbf{q}_{\text{CDW}} = \frac{3}{13}\mathbf{a}^* + \frac{1}{13}\mathbf{b}^*$. Therefore, if we neglect the enhancement of nesting, one can find the area of \mathbf{q} -points with large γ is centered at the reported \mathbf{q}_{CDW} . For 1T-TaTe₂, the large γ area is strongly broadened and expands to ΓK , which is coinciding with the phonon instability area shown in Fig. 3. Meanwhile, χ' and χ'' show small value in the place between Γ and K. Therefore, we can conclude that the \mathbf{q} -dependent electron-phonon coupling induced PLD, instead of Fermi surface nesting, is responsible for CDW in 1T-TaSe_{2-x}Te_x system.

In order to explain the suppression of CDW upon Te doping, we calculated the simplest

hypothetical sample 1*T*-TaSeTe with an ordered stacking of Se/Ta/Te, which is represented as 1*T*-TaSeTe(O). For comparison, we calculated the isostructural 1*T*-TaSSe(O), in which the ordered stacking of S/Ta/Se is experimentally demonstrated³³. Both the phonon dispersions of 1*T*-TaSeTe(O) and 1*T*-TaSSe(O) show the CDW instability (Fig. 4), which means if the S/Se or Se/Te are orderly distributed, CDW could not be suppressed. Therefore, our observed suppression of CDW is due to the doping induced disorder. From Table I, one can notice that the optimized *z*-coordinates of X atoms in pristine 1*T*-TaX₂ (X = Se, Te) is about ±0.27. However, for 1*T*-TaSeTe(O), the *z*-coordinates of X atoms change to $z_{\text{Se}} = 0.249$ and $z_{\text{Te}} = -0.296$, which indicates the TaX₆ octahedra are largely distorted. When the Se and Te atoms are randomly mixed, random distortions of TaX₆ octahedra can be expected in reality, leading to the puckered Ta-Ta layers. This is not compatible with pure two-dimensional PLD. The above scenario can account for the fact that the disorder completely suppresses CDW in 1*T*-TaSe_{2-x}Te_x system.

We also try to understand the superconductivity near CDW based on the PLD mechanism. The electron-phonon coupling strength for each mode ($\lambda_{q\nu}$) is defined as,

$$\lambda_{q\nu} = \frac{\gamma_{q\nu}}{\pi \hbar N(e_{\mathbf{F}}) \omega_{q\nu}^2}. \quad (1)$$

An imaginary frequency ω of the phonon mode indicates the dynamical instability (in our cases it indicates the CDW distortion). When the CDW is suppressed, the stabilizing of 1*T* structure will make the imaginary frequency ω around \mathbf{q}_{CDW} become a small real value^{31,32}. The large γ and small real ω in Eq.(1) can cause a large electron-phonon coupling constant, leading to the superconductivity. However, it is still hard to understand the part of superconducting phase locating inside the CDW area of the phase diagram.

UNIVERSAL SCHEMATIC PHASE DIAGRAMS

1*T*-TaS₂ and 1*T*-TaSe₂ have the same CCDW ground state, but the CDW transitions in them are different. For 1*T*-TaSe₂, just like most TMDs, ICCDW seems to emerge only when CCDW is fully suppressed. On the contrary, in 1*T*-TaS₂ when CCDW is suppressed, domain walls instantly emerge and cut the previous long range CCDW into CCDW domains, leading to NCCDW state. The CCDW domains gradually shrink, while ICCDW grows in interdomain areas. When the CCDW domains disappear, the system transforms to ICCDW

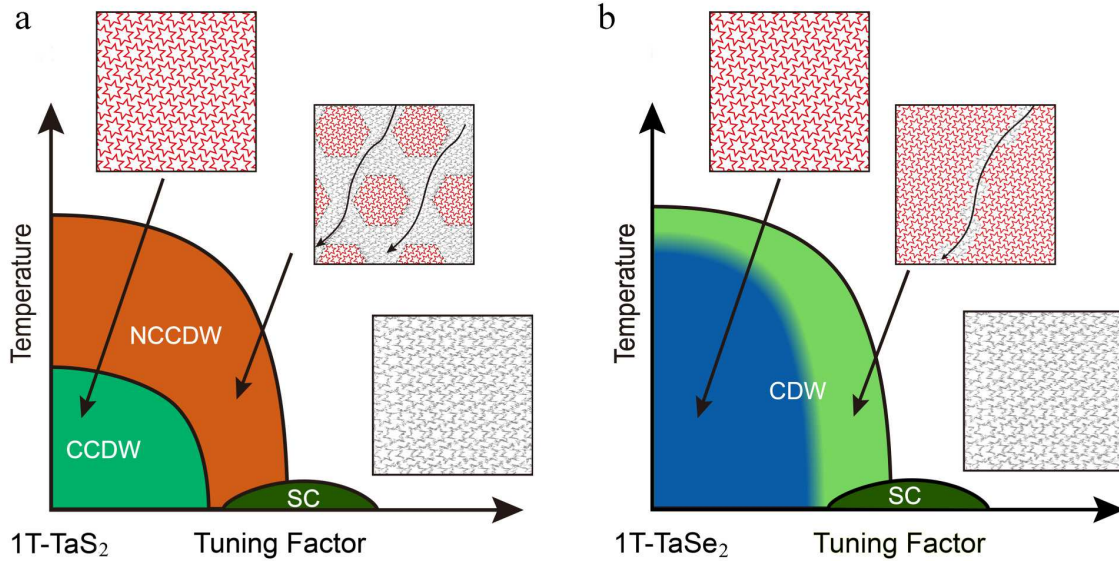


FIG. 5. **Universal schematic phase diagrams.** The schematic tuning phase diagrams of (a) $1T$ -TaS₂ and (b) $1T$ -TaSe₂.

state. That characteristic makes $1T$ -TaS₂ very unique among the TMDs with CDW in a long time⁶.

In CCDW states of $1T$ -TaS₂ and $1T$ -TaSe₂, the $5d$ band of Ta opens a Mott gap, which should prohibit the superconductivity inside CCDW phase. In NCCDW state of $1T$ -TaS₂, the CCDW domains remain Mott insulating, superconductivity can only emerge in the metallic interdomain area⁸. In our present $1T$ -TaSe_{2-x}Te_x, considering the observed very small superconducting volume inside the CDW phase, one can expect that the domain walls emerge when CDW is suppressed, just like the case demonstrated in $1T$ -TiSe₂ under pressure²⁰. Very recently, the coexistence of CCDW and ICCDW phases was observed during the photoinduced suppression of CDW in $1T$ -TaSe₂⁴², which supports our concluded scenario. Since dome-like superconductivity is usually found in TMDs with CDW, the domain walls should be universal, although they are hard to be reflected in the routine measurements.

Thus we can illustrate the universal natures of CDW and related superconductivity in some novel TMDs such as $1T$ -TaS₂, $1T$ -TaSe₂ and $1T$ -TiSe₂. At \mathbf{q}_{CDW} , the strong electron-phonon coupling largely softens the phonon modes. Below T_{CDW} the phonon energy at \mathbf{q}_{CDW} becomes imaginary, meaning there is a new lattice structure. Since CDW originates from

the strong \mathbf{q} -dependent electron-phonon coupling induced PLD instead of the Fermi surface nesting, the CDW gap does not need to be opened exactly at E_F when the CDW transition happens. Therefore, there is no reason to have a metal-insulator transition associated with the CDW transition⁴¹.

We drew the schematic phase diagrams to show the tuning process of CDW in those systems (Fig. 5). The tuning factor such as doping or pressure can harden the phonon mode at \mathbf{q}_{CDW} . When the phonon energy at \mathbf{q}_{CDW} becomes real, CDW is suppressed. The suppression probably firstly happens in a small area, leading to the emergence of domain walls. In $1T$ -TaS₂, the interdomain areas grow and the domains shrink upon tuning. When the domains disappear, the CDW is fully suppressed (Fig. 5 (a)). For $1T$ -TaSe₂ and $1T$ -TiSe₂, in CDW order the domain walls are strongly pinned. In that case, the volumes of the filament-like interdomain areas are very small, so that the routine phase diagram (Fig. 2 (e)) based on transport measurements cannot reflect the situation. A more accurate phase diagram obtained by some measurements with high resolution should follow the schematic diagram presented in Fig. 5 (b). The mechanism of different pinning of domain walls in $1T$ -TaSe₂ and other systems needs to be further investigated.

The superconductivity near CDW is not due to QCP, but to the emergence of domain walls. In the interdomain areas, as CDW is just suppressed, the phonon frequency at \mathbf{q}_{CDW} has a small real value, leading to a large total electron-phonon coupling constant. Once the interdomain areas percolated, superconductivity emerges (Fig. 5). When system is far away from CDW, the phonon frequency at \mathbf{q}_{CDW} become larger, and thus the total electron phonon coupling constant decreases. Therefore, a dome-like superconducting phase can be obtained.

In conclusion, we prepared a series of $1T$ -TaSe_{2-x}Te_x ($0 \leq x \leq 2$) single crystals and summarized an overall electronic phase diagram through the transport measurements. The CDW in $1T$ -TaSe_{2-x}Te_x ($0 \leq x \leq 2$) is gradually suppressed by Te doping induced Se/Te disorder and finally disappears when $x > 0.5$. A dome-like superconducting phase with the maximum T_c^{onset} of 2.5 K is observed near CDW. The superconducting volume is very small inside the CDW phase and becomes very large instantly when CDW is fully suppressed. Based on the first principle calculations, we found that the origin of CDW in the system should be the strong \mathbf{q} -dependent electron-phonon coupling induced PLD instead of Fermi surface nesting. In this framework the natures of CDW and superconductivity can be well

understood. The volume variation of superconductivity implies the emergence of domain walls in the suppressing process of CDW. Our concluded scenario makes a fundamental understanding about CDW and related superconductivity in TMDs.

METHODS

The single crystals were grown via the chemical vapor transport (CVT) method with iodine as a transport agent. The high-purity elements Ta (4N), Se(4N), and Te(5N) were mixed in chemical stoichiometry, and heated at 900°C for 4 days in an evacuated quartz tube. The harvested $\text{TaSe}_{2-x}\text{Te}_x$ powders and iodine (density: 5 mg/cm³) were then sealed in another quartz tube and heated for two weeks in a two-zone furnace, where the temperature of source and growth zones were fixed at 950°C and 850°C, respectively. Finally, the tubes were rapidly quenched in cold water to ensure retaining of the 1T phase.

The X-ray diffraction (XRD) patterns were obtained on a Philips X'pert PRO diffractometer with Cu K_α radiation ($\lambda = 1.5418 \text{ \AA}$). Structural refinements were performed by using Rietveld method with the X'pert HighScore Plus software. Electron diffraction and HAADF-STEM experiments were performed in the JEOL ARM200F equipped with double aberration correctors and cold field emission gun operated at 200 kV. For the STEM images, the convergence angle is 28 mrad and the collection angle of the HAADF detector is between 90 and 370 mrad. Under this condition, the spatial resolution is about 0.08 nm. The electrical resistivity was measured in the ab plane of each crystal in zero applied magnetic field by the standard four-probe ac technique using the Quantum Design Physical Property Measurement System (PPMS). The four 50 μm diameter platinum wire electrical leads were attached to the crystals' tape-tripped fresh surface using silver epoxy. Measurement of the temperature dependence of magnetic susceptibility and the isothermal hysteresis loop were carried out in the Quantum Design Magnetic Property Measurement System (MPMS) equipped with a ³He cryostat.

The first principles calculations based on density functional theory (DFT) were carried out using QUANTUM ESPRESSO package⁴³ with ultrasoft pseudopotentials. The exchange-correlation interaction was treated with the local-density-approximation (LDA) according to Perdew and Zunger⁴⁴. The energy cutoff for the plane-wave basis set was 35 Ry. Brillouin zone sampling is performed on the Monkhorst-Pack (MP) mesh⁴⁵ of $32 \times 32 \times 8$. The

Vanderbilt-Marzari Fermi smearing method with a smearing parameter of $\sigma = 0.02$ Ry was used for the calculations of the total energy and electron charge density. Phonon dispersions were calculated using DFPT⁴⁶ with an $8 \times 8 \times 4$ mesh of \mathbf{q} -points. In order to investigate the distribution of CDW instability around the \mathbf{q}_{CDW} , $16 \times 16 \times 1$ \mathbf{q} -points were used. Denser $64 \times 64 \times 8$ \mathbf{k} -points are used for electron-phonon coupling.

The real part of the electron susceptibility is defined as

$$\chi'(\mathbf{q}) = \sum_{\mathbf{k}} \frac{f(\varepsilon_{\mathbf{k}}) - f(\varepsilon_{\mathbf{k}+\mathbf{q}})}{\varepsilon_{\mathbf{k}} - \varepsilon_{\mathbf{k}+\mathbf{q}}}, \quad (2)$$

where $f(\varepsilon_{\mathbf{k}})$ is Fermi-Dirac function. The imaginary part is²⁴

$$\chi''(\mathbf{q}) = \sum_{\mathbf{k}} \delta(\varepsilon_{\mathbf{k}} - \varepsilon_{\mathbf{F}}) \delta(\varepsilon_{\mathbf{k}+\mathbf{q}} - \varepsilon_{\mathbf{F}}). \quad (3)$$

We used a mesh of approximately 40,000 \mathbf{k} points in the full reciprocal unit cell to calculate the energy eigenvalues derived for the electron susceptibilities.

The phonon linewidth γ is defined by

$$\gamma_{q\nu} = 2\pi\omega_{q\nu} \sum_{ij} \int \frac{d^3k}{\Omega_{BZ}} |g_{q\nu}(\mathbf{k}, i, j)|^2 \times \delta(\varepsilon_{\mathbf{q},i} - \varepsilon_{\mathbf{F}}) \delta(\varepsilon_{\mathbf{k}+\mathbf{q},j} - \varepsilon_{\mathbf{F}}), \quad (4)$$

where the electron-phonon coefficients $g_{q\nu}(\mathbf{k}, i, j)$ are defined as,

$$g_{q\nu}(\mathbf{k}, i, j) = \left(\frac{\hbar}{2M\omega_{q\nu}}\right)^{1/2} \langle \psi_{i,\mathbf{k}} | \frac{dV_{\text{SCF}}}{d\hat{u}_{q\nu}} \cdot \hat{\varepsilon}_{q\nu} | \psi_{j,\mathbf{k}+\mathbf{q}} \rangle. \quad (5)$$

According to this definition, γ , which reflects the electron-phonon coupling contribution, is a quantity that does not depend on real or imaginary nature of the phonon frequency.

* The authors contributed equally to this work.

† Corresponding author: wjlu@issp.ac.cn

‡ Corresponding author: hxyang@iphy.ac.cn

§ Corresponding author: ypsun@issp.ac.cn

¹ Mathur, N. D., Grosche F. M., Julian S. R., Walker I. R., Freye D. M., Haselwimmer R. K. W. & Lonzarich G. G. Magnetically mediated superconductivity in heavy fermion compounds. *Nature* **394**, 39-43 (1998).

² Tranquada J. M., Sternlieb B. J., Axe J. D., Nakamura Y. & Uchida S. Evidence for stripe correlations of spins and holes in copper oxide superconductors. *Nature* **375**, 561-563 (1995).

- ³ Canfield P. C. & Budko S. L. Superconductivity: a case study of the effects of transition metal doping on BaFe₂As₂. *Annu. Rev. Condens. Matter Phys.* **1**, 27-50 (2010).
- ⁴ Sidorov V. A., Nicklas M., Pagliuso P. G., Sarrao J. L., Bang Y., Balatsky A. V. & Thompson J. D. Superconductivity and quantum criticality in CeCoIn₅. *Phys. Rev. Lett.* **89**, 157004 (2002).
- ⁵ Tallon J. L., Loram J. W., Williams G. V. M., Cooper J. R., Fisher I. R., Johnson J. D., Staines M. P. & Bernhard C. Critical doping in overdoped high- T_c superconductors: a quantum critical point? *Phys. Stat. Sol. B* **215**, 531-540 (1999).
- ⁶ Wilson J. A., Di Salvo F. J. & Mahajan S. Charge-density waves and superlattices in the metallic layered transition metal dichalcogenides. *Adv. Phys.* **24**, 1171-1248 (1975).
- ⁷ Yu Y. J., Yang F. Y., Lu X. F., Yan Y. J., Cho Y.-H., Ma L. G., Niu X. H., Kim S., Son Y.-W., Feng D. L., Li S. Y., Cheong S.-W., Chen X. H. & Zhang Y. B. Gate-tunable phase transitions in thin flakes of 1T-TaS₂. *Nat. Nanotechnol.* **10**, 270 (2015).
- ⁸ Sipos B., Kusmartseva A. F., Akrap A., Berger H., Forró L. & Tutiš E. From Mott state to superconductivity in 1T-TaS₂. *Nature Mater.* **7**, 960-965 (2008).
- ⁹ Morosan E., Zandbergen H. W., Dennis B. S., Bos J. W. G., Onose Y., Klimczuk T., Ramirez A. P., Ong N. P. & Cava R. J. Superconductivity in Cu_xTiSe₂. *Nature Phys.* **2**, 544-550 (2006).
- ¹⁰ Morosan E., Wagner K. E., Zhao L. L., Hor. Y., Williams A. J., Tao J., Zhu Y. & Cava R. J. Multiple electronic transitions and superconductivity in Pd_xTiSe₂. *Phys. Rev. B* **81**, 09424 (2010).
- ¹¹ Wagner K. E., Morosan E., Hor Y. S., Tao J., Zhu Y., Sanders T., McQueen T. M. & Cava R. J. Tuning the charge density wave and superconductivity in Cu_xTaS₂. *Phys. Rev. B* **78**, 104520 (2008).
- ¹² Li L. J., Lu W. J., Zhu X. D., Ling L. S., Qu Z. & Sun Y. P. Fe-doping-induced superconductivity in the charge-density-wave system 1T-TaS₂. *Europhys. Lett.* **97**, 67005 (2012).
- ¹³ Ang R., Tanaka Y., Ieki E., Nakayama K., Sato T., Li L. J., Lu W. J., Sun Y. P. & Takahashi T. Real-space coexistence of the melted Mott state and superconductivity in Fe-substituted 1T-TaS₂. *Phys. Rev. Lett.* **109**, 176403 (2012).
- ¹⁴ Liu Y., Ang R., Lu W. J., Song W. H., Li L. J. & Sun Y. P. Superconductivity induced by Se-doping in layered charge-density-wave system 1T-TaS_{2-x}Se_x. *Appl. Phys. Lett.* **102**, 192602 (2013).
- ¹⁵ Ang R., Miyata Y., Ieki E., Nakayama K., Sato T., Liu Y., Lu W. J., Sun Y. P. & Takahashi T.

- Superconductivity and bandwidth-controlled Mott metal-insulator transition in $1T$ -TaS_{2-x}Se_x. *Phys. Rev. B* **88**, 115145 (2013).
- ¹⁶ Liu Y., Li L. J., Lu W. J., Ang R., Liu X. Z. & Sun Y. P. Coexistence of superconductivity and commensurate charge density wave in $4H_b$ -TaS_{2-x}Se_x. *J. Appl. Phys.* **115**, 043915 (2014).
- ¹⁷ Kusmartseva A. F., Sipos B., Berger H., Forró L. & Tutiš E. Pressure induced superconductivity in pristine $1T$ -TiSe₂. *Phys. Rev. Lett.* **103**, 236401 (2009).
- ¹⁸ Li S. Y., Wu G., Chen X. H. & Taillefer L. Single-gap s-wave superconductivity near the charge-density-wave quantum critical point in Cu_xTiSe₂. *Phys. Rev. Lett.* **99**, 107001 (2007).
- ¹⁹ Barath H., Kim M., Karpus J. F., Cooper S. L., Abbamonte P., Fradkin E., Morosan E. & Cava R. J. Quantum and classical mode softening near the charge-density-wave-superconductor transition of Cu_xTiSe₂. *Phys. Rev. Lett.* **100**, 106402 (2008).
- ²⁰ Joe Y. I., Chen X. M., Ghaemi P., Finkelstein K. D., de la Pena G. A., Gan Y., Lee J. C. T., Yuan S., Geck J., MacDougall G. J., Chiang T. C., Cooper S. L., Fradkin E. & Abbamonte P. Emergence of charge density wave domain walls above the superconducting dome $1T$ -TiSe₂. *Nature Phys.* **10**, 421-425 (2014).
- ²¹ Peierls R. E. Quantum Theory of Solids (Oxford, 1955).
- ²² Peierls R. E. More Surprises in Theoretical Physics (Princeton University Press, 1991).
- ²³ Fröhlich H. On the theory of superconductivity: the one-dimensional case. *Proc. R. Soc. A* **233**, 296 (1954).
- ²⁴ Johannes M. D. & Mazin I. I. Fermi surface nesting and the origin of charge density waves in metals. *Phys. Rev. B* **77**, 165135 (2008).
- ²⁵ Chan S.-K. & Heine V. Spin density wave and soften phonon mode from nesting Fermi surfaces. *J. Phys. F: Metal Phys.* **3**, 795-809 (1973).
- ²⁶ Tanda S., Sambongi T., Tani T. & Tanaka S. X-ray study of charge density wave structure in $1T$ -TaS₂. *J. Phys. Soc. Jpn.* **53**, 476-479 (1984).
- ²⁷ Myron H. W. & Freeman A. J. Electronic structure and Fermi-surface-related instabilities in $1T$ -TaS₂ and $1T$ -TaSe₂. *Phys. Rev. B* **11**, 2735-2379 (1975).
- ²⁸ Myron H. W., Rath J. & Freeman A. J. Generalized electronic susceptibility and charge-density waves in $1T$ -TaS₂ and $1T$ -TaSe₂. *Phys. Rev. B* **15**, 885-889 (1977).
- ²⁹ Battaglia C., Cercellier H., Clerc F., Despont L., Garnier M. G., Koitzsch C. & Aebi P. Fermi-surface-induced lattice distortion in NbTe₂. *Phys. Rev. B* **72**, 195114 (2005).

- ³⁰ Sharma S., Nordström L. & Johansson B. Stabilization of charge-density waves in $1T$ - TaX_2 ($X = \text{S}, \text{Se}, \text{Te}$): First-principles total energy calculations. *Phys. Rev. B* **66**, 195101 (2002).
- ³¹ Liu A. Y. Electron-phonon coupling in compressed $1T$ - TaS_2 : stability and superconductivity from first principles. *Phys. Rev. B* **79**, 220515(R) (2009).
- ³² Ge Y. & Liu A. Y. First-principle investigation of the charge-density-wave instability in $1T$ - TaSe_2 . *Phys. Rev. B* **82**, 155133 (2010).
- ³³ Ang R., Wang Z. C., Chen D. L., Tang J., Liu N., Liu Y., Lu W. J., Sun Y. P., Mori T. & Ikuhara Y. Atomistic origin of an ordered superstructure induced superconductivity in layered chalcogenides. *Nat. Commun.* **6**, 6091 (2015).
- ³⁴ Luo H. X., Xie W. W., Tao J., Inoue H., Gyenis A., Krizan J. W., Yazdani A., Zhu Y. & Cava R. J. Polytypism, polymorphism, and superconductivity in $\text{TaSe}_{2-x}\text{Te}_x$. *Proc. Natl. Acad. Sci. USA* **112**, 1174-1180 (2015).
- ³⁵ Johannes M. D., Mazin I. I. & Howells C. A. Fermi-surface nesting and the origin of the charge-density wave in NbSe_2 . *Phys. Rev. B* **73**, 205102 (2006).
- ³⁶ Ge Y. & Liu A. Y. Effect of dimensionality and spin-orbit coupling on charge-density-wave transition in $2H$ - TaSe_2 . *Phys. Rev. B* **86**, 104101 (2012).
- ³⁷ Calandra M. & Mauri F. Charge-density wave and superconducting dome in TiSe_2 from electron-phonon interaction. *Phys. Rev. Lett.* **106**, 196406 (2011).
- ³⁸ Woolley A. M. & Wexler G. Band structures and Fermi surfaces for $1T$ - TaS_2 , $1T$ - TaSe_2 and $1T$ - VSe_2 . *J. Phys. C: Solid State Phys.* **10**, 2601-2616 (1977).
- ³⁹ Bovet M., Popović D., Clerc F., Koitzsch C., Probst U., Bucher E., Berger H., Naumović D. & Aebi P. Pseudogapped Fermi surfaces of $1T$ - TaS_2 and $1T$ - TaSe_2 : a charge density wave effect. *Phys. Rev. B* **69**, 125117 (2004).
- ⁴⁰ Yu X. L., Liu D. Y., Lin H.-Q., Jia T. & Zou L.-J. arXiv: 1407.1407 (2014).
- ⁴¹ Zhu X. T., Cao Y. W., Zhang J. D., Plummer E. W. & Guo J. D. Classification of charge density waves based on their nature. *Proc. Natl. Acad. Sci. USA* **112**, 2367-2371 (2015).
- ⁴² Sun S. S., Wei L. L., Li Z. W., Cao G. L., Liu Y., Lu W. J., Sun Y. P., Tian H. F., Yang H. X., & Li J. Q. Direct observation of an optically induced charge density wave transition in $1T$ - TaSe_2 . *Phys. Rev. B* **92**, 224303 (2015).
- ⁴³ Giannozzi P., Baroni S., Bonini N., Calandra M., Car R., Cavazzoni C., Ceresoli D., Chiarotti G. L., Cococcioni M., Dabo I., Corso A. D., de Gironcoli S., Fabris S., Fratesi G., Gebauer

- R., Gerstmann U., Gougoussis C., Kokalj A., Lazzeri M., M.-Samos L., Marzari N., Mauri F., Mazzarello R., Paolini S., Pasquarello A., Paulatto L., Sbraccia C., Scandolo S., Sclauzero G., Seitsonen A. P., Smogunov A., Umari P. & Wentzcovitch R. M. QUANTUM ESPRESSO: a modular and open-source software project for quantum simulations of materials. *J. Phys.: Condens. Matter* **21**, 395502 (2009).
- ⁴⁴ Perdew J. P. & Zunger A. Self-interaction correction of density-functional approximations for many-electron systems. *Phys. Rev. B* **23**, 5048-5079 (1981).
- ⁴⁵ Monkhorst H. J. & Pack J. D. Special points for Brillouin-zone integrations. *Phys. Rev. B* **13**, 5188-5192 (1976).
- ⁴⁶ Baroni S., de Gironcoli S., Corso A. D. & Giannozzi P. Phonons and related crystal properties from density-functional perturbation theory. *Rev. Mod. Phys.* **73**, 515-562 (2001).

ACKNOWLEDGEMENTS

This work was supported by the National Key Basic Research under Contract No. 2011CBA00111, the National Nature Science Foundation of China under Contract Nos. 11404342, 11274311 and 11190022, the National Basic Research Program of China under Contract 2015CB921300, the Joint Funds of the National Natural Science Foundation of China and the Chinese Academy of Sciences Large-scale Scientific Facility (Grand No. U1232139), Anhui Provincial Natural Science Foundation under Contract No. 1408085MA11, and the Directors Fund under Contract No. YZJJ201311 of Hefei Institutes of Physical Science, Chinese Academy of Sciences.

AUTHOR CONTRIBUTIONS

Y.L., L.J.L. and Y.P.S. synthesized the single crystals and carried out the XRD measurement. H.F.T., H.X.Y. and J.Q.L. performed the HAADF-STEM experiments. Y.L., X.D.Z. C.Y.X., L.P., P.T., W.H.S., L.S.L., X.B.Z. and Y.P.S performed the transport and magnetization measurements. D.F.S., R.C.X. and W.J.L. carried out the DFT calculations and explain the experimental observation. Y.L., D.F.S., W.J.L. and Y.P.S. drafted the manuscript. All authors reviewed and approved the manuscript.

COMPETING FINANCIAL INTERESTS

The authors declare no competing interests.